Mooring observations and numerical modeling of thermal structures in the South China Sea

Ya-Ting Chang,[1] Tswen Yung Tang,[1] Shenn-Yu Chao,[2] Ming-Huei Chang,[3] Dong S. Ko,[4] Yiing Jang Yang,[5] Wen-Der Liang,[5] and Michael J. McPhaden[6]

[1] Three sets of Autonomous Temperature Line Acquisition Systems were deployed in the South China Sea. Gaps aside, the data covered nearly 3 years at the northern station and about 2 years farther south. Fluctuations ranged from episodic to interannual. Internal tides, more diurnal than semidiurnal, were active basinwide. Twelve typhoons passed during measurement periods. The most severe one, typhoon Babs in 1998, caused a temperature drop of over 7°C at 50 m. Despite strong monsoons, only near-surface temperature showed clear seasonal variations. Intraseasonal variations induced by mesoscale eddy stood out much better at subsurface depths. Propagating eddies aside, some eddies were seasonal and nearly stationary. From daily archives of an eddy-resolving, data-assimilating ocean model (East Asian Seas Nowcast/Forecast System), we identified two paradigms leading to the generation of a persistent spring-summer warm eddy in the central-western basin. In normal years, a complete cyclonic gyre was driven by a strong winter northeast monsoon. Water piled up along the periphery of the South China Sea. Afterward, a warm eddy could be generated from west of Luzon Island and propagated westward while intensifying. Under a weak northeast monsoon, such as in El Niño years, piled-up water tended to stay in the southern basin. When the wind relaxed in spring, warm water returned northward to form a warm eddy in the central-western basin. Transition from SW to NE monsoon also often led to a warm eddy generation in southern latitudes, when the summer eastward jet departing from central Vietnam broke up.

1. Introduction

[2] The South China Sea (SCS), the largest marginal sea in the tropics, is a deep basin with a mostly shallow perimeter (Figure 1). Shallow passages to surrounding seas aside, the Luzon Strait, about 400 km wide and 2000 m deep, is the only major pathway connecting it to the Pacific Ocean. Monsoon winds, southwest in summer and northeast in winter, drive the seasonally varying, basinwide circulation [*Wyrtki*, 1961]. Built around this central theme, subsequent studies before the satellite altimeter era, either through numerical modeling [*Shaw and Chao*, 1994; *Chu et al.*, 1998; *Shaw et al.*, 1996; *Chao et al.*, 1996] or data analysis [*Qu*, 2000; *Shaw et al.*, 1996], revealed more details. In essence, the monsoon winds produce a basinwide cyclonic gyre in winter and double gyres in summer, cyclonic in the north and anticyclonic in the south. The Earth's β effect plays a role and, in consequence, these gyres tend to intensify along the western boundary. Some seasonal eddies were also evident from these early studies. For example, a cyclonic eddy northwest of Luzon Island occurred in winter and another one east of Vietnam occurred in summer [*Shaw et al.*, 1996; *Qu*, 2000]. During the seasonal monsoon transition, there is a warm pool in the central SCS in spring that becomes a cold pool in fall [*Chu et al.*, 1997, 1998].

[3] In recent years, satellite altimeter data availability and increasingly realistic numerical simulations heightened the awareness of energetic eddy activities in the region. Some eddies are seasonal and nearly stationary while others propagate like first baroclinic mode Rossby waves [*Morimoto et al.*, 2000]. In summer, a pair of counterrotating eddies (i.e., a dipole) off central Vietnam, cyclonic to the north and anticyclonic to the south, seemingly propels an eastward jet in between to separate from the coast of Vietnam

[1]Institute of Oceanography, National Taiwan University, Taipei, Taiwan.
[2]Horn Point Laboratory, University of Maryland Centers for Environmental Science, Cambridge, Maryland, USA.
[3]Department of Marine Environmental Informatics, National Taiwan Ocean University, Keelung, Taiwan.
[4]Naval Research Laboratory, Oceanography Division, Ocean Dynamics and Prediction Branch, Stennis Space Center, Mississippi, USA.
[5]Department of Marine Science, Naval Academy, Kaohsiung, Taiwan.
[6]Pacific Marine Environmental Laboratory, National Ocean and Atmosphere Administration, Seattle, Washington, USA.
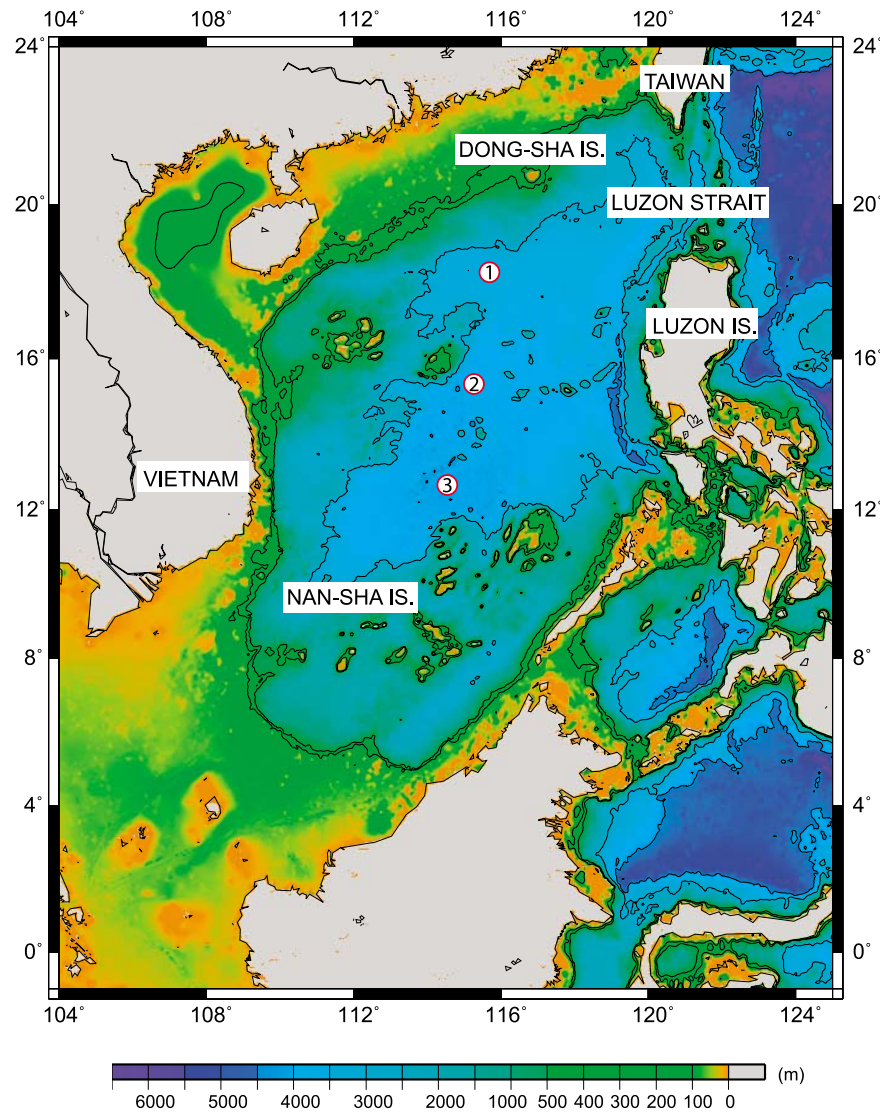
Figure 1. ATLAS buoy stations (SCS1, SCS2, and SCS3) and bathymetry in the South China Sea.

near 13°N [*Bayler and Liu*, 2008]. Statistics from a 5 year satellite altimetry data set tells more. In general, the SCS eddies are geographical and polarity sensitive; they favor regions north of 10°N [*Wang et al.*, 2000] and anticyclonic rotation [*Wang et al.*, 2003]. In the northeastern SCS, the encroaching Kuroshio can also induce mesoscale eddies of either polarity [*Wu et al.*, 2005; *Wu and Chiang*, 2007].

[4] Summer tropical cyclones and typhoons are frequent. They come mostly from the Pacific Ocean. Fewer are from the Indian Ocean or spun off locally. Though mostly confined by shallow peripheries, the typhoon-induced SCS response still retains essential open-ocean characteristics as documented in *Price* [1981] and *Price et al.* [1994]. For example, the modeled response to tropical cyclone Ernie still contains a cold wake and trailing clockwise inertial current [*Chu et al.*, 2000]. Observationally, sea surface cooling in the northern SCS induced by typhoon Kai-Tak ranged up to 9°C in the cold wake [*Lin et al.*, 2003; *Tseng et al.*, 2010]. The larger-than-normal temperature drop owes

its occurrence to slow translation speed, oceanic stratification, and bathymetry-induced upwelling [*Tseng et al.*, 2010].

[5] Barotropic tides are predominantly diurnal in the SCS [*Mazzega and Bergé*, 1994; *Yanagi et al.*, 1997; *Beardsley et al.*, 2004; *Jan et al.*, 2007]. Their amplitudes in the deep basin are understandably small [*Fang et al.*, 1999]. In contrast, internal tides, whether diurnal or semidiurnal, are quite energetic [*Duda et al.*, 2004; *Lynch et al.*, 2004; *Ramp et al.*, 2004]. Models suggest their vitality even in the deep basin of the northern SCS [*Niwa and Hibiya*, 2004]. Internal tides originate from Luzon Strait, propagate westward across the northern SCS basin and dissipate thereafter over the continental slope and shelf in the western reaches of the northern SCS [*Niwa and Hibiya*, 2004; *Chang et al.*, 2006].

[6] El Niño/Southern Oscillation (ENSO) manifests itself as interannual warm events in the SCS [*Chao et al.*, 1996; *Xie et al.*, 2003]. The warmer sea surface results from weaker surface circulation under weaker seasonal monsoon
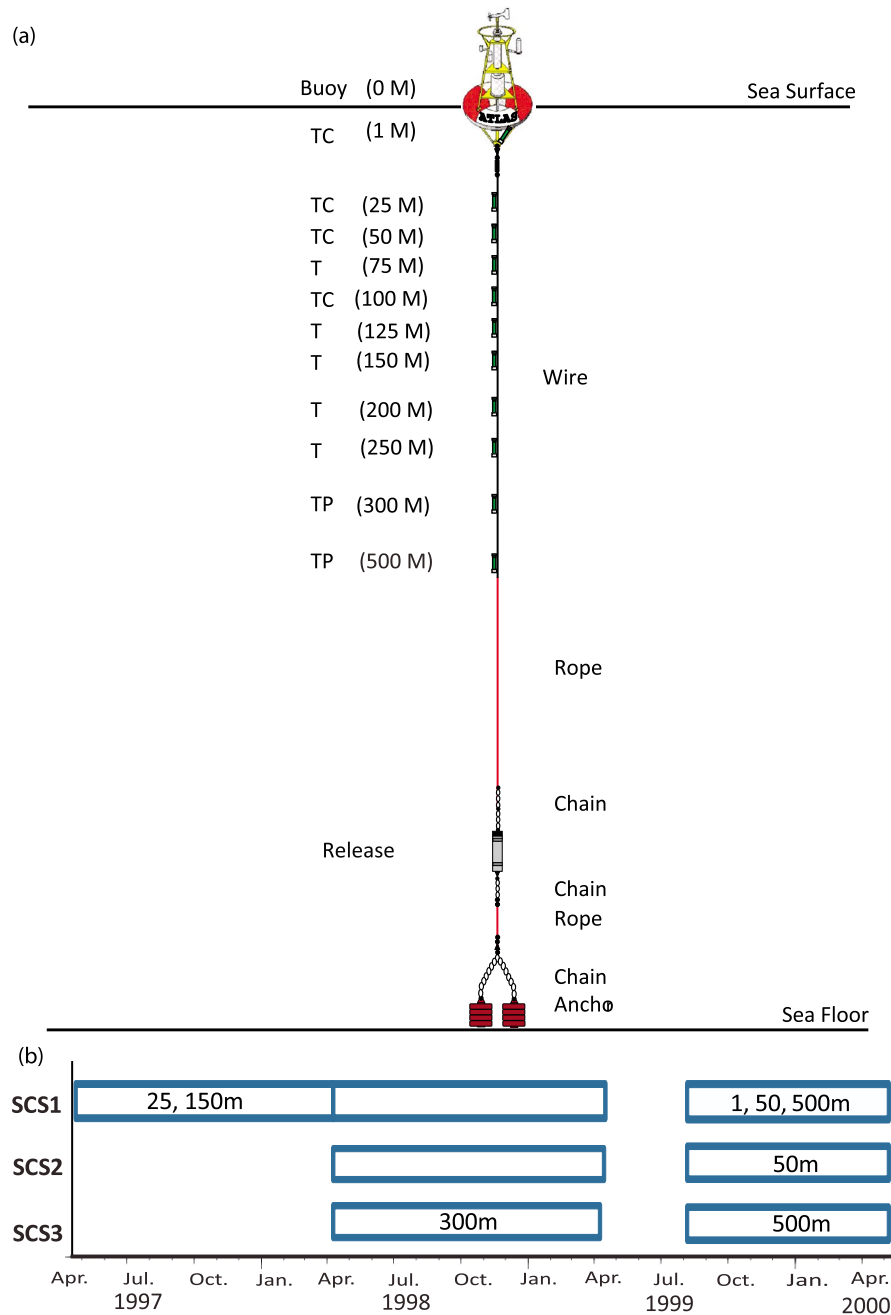
Figure 2. (a) ATLAS mooring design: T, temperature sensor, TC, temperature-conductivity sensor, TP, temperature-pressure sensor. (b) Periods of deployment and depths of lost data in each period.

forcing [*Chao et al.*, 1996]. The dipole vortices off Vietnam weaken, as does the eastward jet [*Wu and Chang*, 2005]. Analyzing satellite altimeter data over interannual time scales, the maximum variance often exists off central Vietnam [*Xie et al.*, 2003; *Wu and Chang*, 2005; *Chang et al.*, 2008].

[7] Past observations are gappy in time and, climatological data aside, generally lack central basin measurements. Our Autonomous Temperature Line Acquisition System (ATLAS) buoy observations, to be described in section 2, make up for these deficiencies. Section 3 reports essential results.

Buoy observations lack spatial coverage so we enhance spatial resolution by comparing the mooring observations with concurrent satellite altimeter data. Section 4 analyzes observational results in conjunction with satellite altimeter data and climatology. A comparison with eddy-resolving regional numerical simulations for the same period would be desirable. Unfortunately, a qualified model (East Asian Seas Nowcast/ Forecast System or EASNFS) did not become operational until 2003. It nevertheless serves a useful tool to identify mechanisms leading to our observational findings. Section 5 uses EASNFS archives to discuss the season-sensitive for-
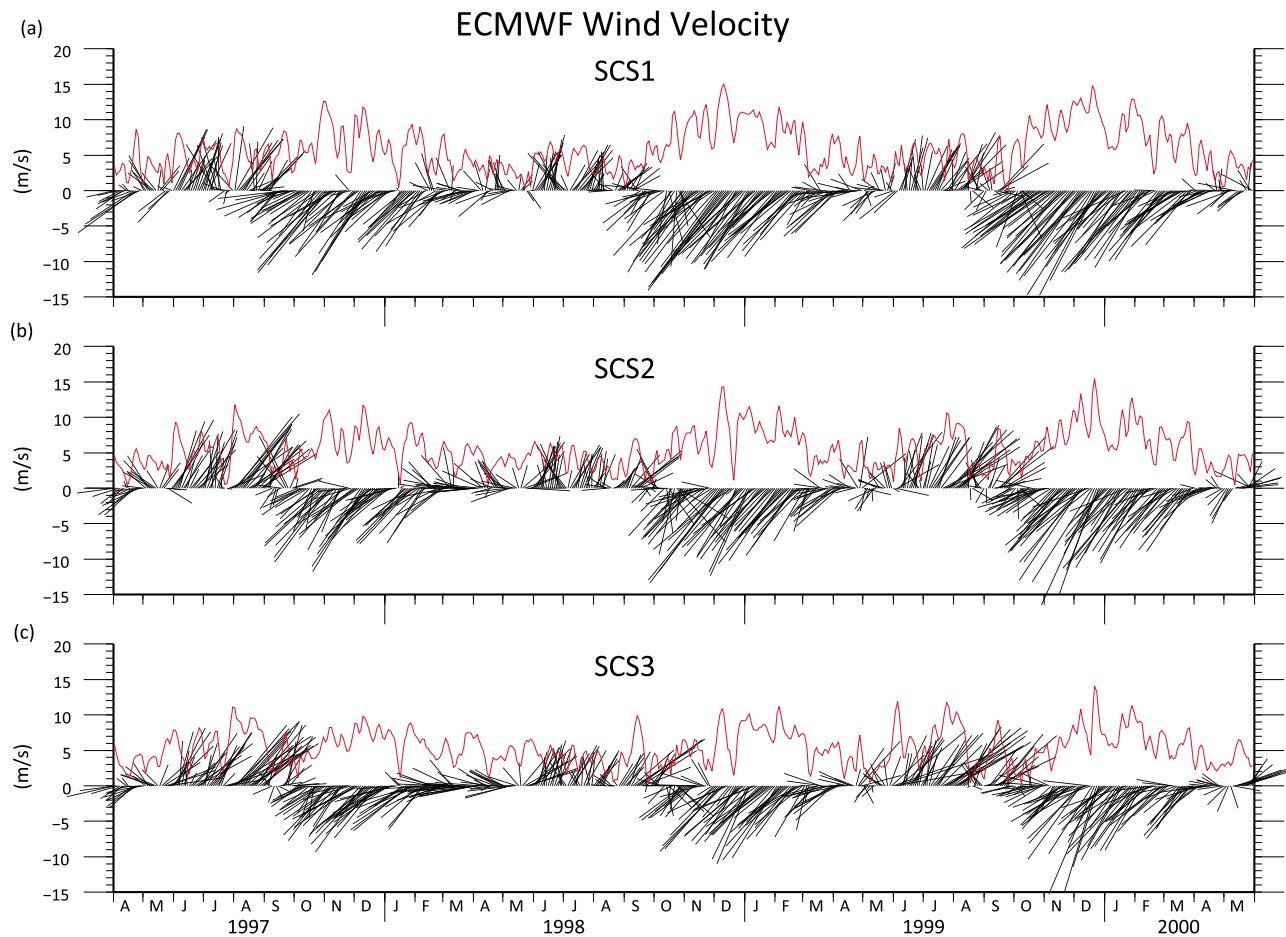
Figure 3. Wind stick (black) diagrams and wind speeds (red) at 10 m height after 96 h low-pass filtration over (a) SCS1, (b) SCS2, and (c) SCS3, from European Centre for Medium-Range Weather Forecasts (ECMWF) 40 Year Re-analysis (ERA-40).

mation of warm eddies in the SCS. A summary is provided in section 6.

2. Field Work

[8] As an oceanographic component of the South China Sea Monsoon Experiment (SCSMEX), we had deployed three ATLAS buoys [*Milburn and McLain*, 1986] in the central SCS basin. Figure 1 shows their locations. With minor deviations, the three stations (SCS1, SCS2, and SCS3) approximately dotted the line between the Dong-Sha Islands (Pratas Islands) and Nan-Sha Islands (Spratly Islands) every one-third of the distance or 330 km. Local water depths at SCS1, SCS2, and SCS3 are 3800, 4250, and 4350 m, respectively. The ATLAS buoy at SCS1 was deployed in April 1997, the beginning of the SCSMEX pilot study, and replaced in April 1998. The remaining two buoys were deployed in April 1998 when the Intensive Observation Period began. All three buoys were recovered in April 1999, redeployed in August 1999, and again retrieved for good in May 2000.

[9] The ATLAS buoys (Figure 2a) were designed and assembled by the Pacific Marine Environmental Laboratory/ National Ocean and Atmosphere Administration (PMEL/ NOAA). Similar buoys have been widely used in the trop-

ical Pacific Ocean to monitor the evolution of ENSO events [*McPhaden et al.*, 1998]. The surface meteorological sensors, data logger, and Argos transmitter were mounted on a 3 m tall tower on top of each buoy. These sensors measured the wind velocity, air temperature, short-wave radiation, rainfall, and humidity. Below the sea surface, there were 11 temperature, 4 conductivity, and 2 pressure sensors to record the upper 500 m ocean thermal structure, salinity, and mooring stability. The 11 temperature sensors were located at 1, 25, 50, 75, 100, 125, 150, 200, 250, 300, and 500 m. The 4 conductivity sensors were at 1, 25, 50, and 100 m. The pressure sensors were located at 300 and 500 m. The subsurface data were internally recorded at 10 min intervals; daily averages were transmitted to the surface data logger, which also stored the raw and daily surface meteorological data.

[10] Shortly after deployments, fishermen vandalized most of the meteorological sensors and Argos transmitters. In consequence, time series of meteorological measurements were generally short and gappy. We therefore excluded meteorological data from discussions below and used ECMWF winds as replacements. Subsurface time series were generally intact except for a few gaps (Figure 2b), possibly caused by tangled fishing lines or sensor malfunction. The conductivity sensors generally lasted for a few
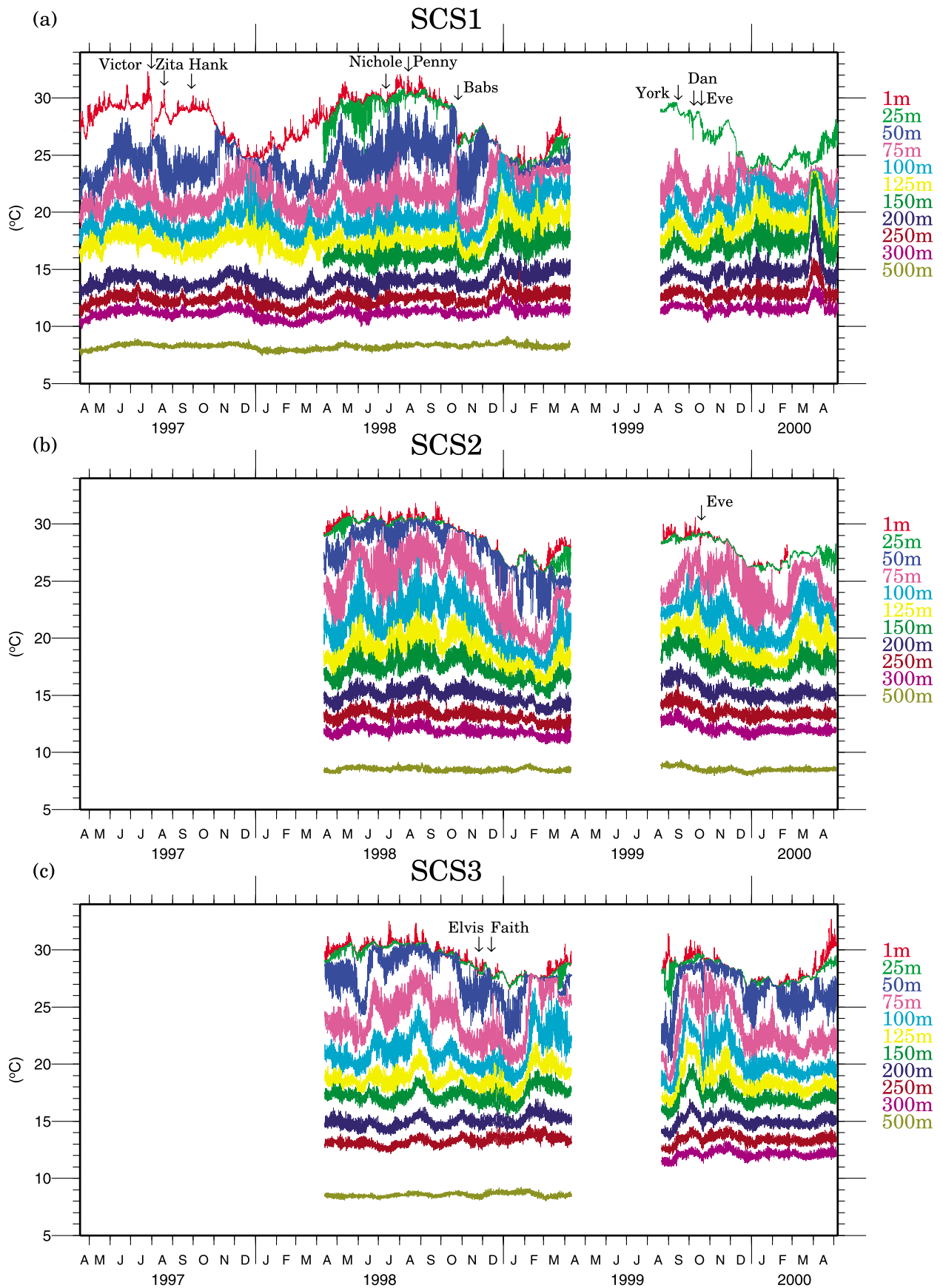
Figure 4

months after deployment. The ATLAS moorings were generally quite stable even under typhoon strength winds. Judging from pressure sensor data (not shown), vertical excursions were generally less than 3 m but could occasionally exceed 10 m under typhoons or unusually strong winter monsoon winds.

3. Data at a Glance

3.1. Winds

[11] In lieu of fragmented time series from buoys, we use winds from *ECMWF* 40 Year Reanalysis [ERA40; *Uppala et al.*, 2005] to facilitate discussions below. After a 96 h low-pass filtration, Figure 3 shows wind vectors and wind speeds over the three moorings at 2 d intervals. Under the influence of the East Asian monsoon system, the wind is southwesterly in summerlike periods and northeasterly in winterlike periods. We refer to winterlike and summerlike periods as those predominated by the northeast and southwest monsoons, respectively. They overlap somewhat with calendar winter and summer but do not exactly begin or end as defined by calendar. In general, the winterlike period is from October to February and the summerlike period is from June to August. Figure 3 shows the predominance and tenacity of NE monsoon. By comparison, the SW monsoon is weaker and fluctuates. The transition from SW monsoon to NE monsoon takes only one month (September). In contrast, the reverse transition takes up to 3 months (from March to May). During onset, the NE monsoon runs over the three moorings from north to south.

[12] Beyond the seasonal time scale, winds at all stations showed clear interannual variations. The NE monsoon was the weakest in the winter of 1997–1998. The SW monsoon was also weaker in summer 1998. Extrapolating from past experiences [*Chao et al.*, 1996], the well-known 1997–1998 El Niño should have been responsible for the weakened monsoons. The NE monsoon in 1999–2000 rebounded (Figure 3) La Niña events in 1998–1999 and 1999–2000.

3.2. Thermal Structure

[13] Figure 4 shows all available time series of temperature at 60 min intervals. Sub-sampling from 10 min to 60 min blurs high-frequency signals a little, but we base our discussions below on the raw data. A few features previously unseen from earlier observations stand out. For example, high-frequency fluctuations were large, persistent, and basinwide. In these deep-ocean settings, the annual cycle was not particularly noticeable at subsurface depths. To the contrary, corresponding intraseasonal fluctuations were large and frequent. Close-up views follow.

3.2.1. Near-surface

[14] At SCS1 (Figure 4a), the seasonal variation of temperature was more noticeable at 1 m, which we refer to as sea surface temperature (SST). It diminished downward at 25 m (T25) and 50 m (T50). SST fluctuations from days to weeks were mostly typhoon related. Daily fluctuations due to either tides or the diurnal heating cycle were generally small. The SST time series began from a seasonal warming phase. The would-be monotonic increase from May to August 1997 was occasionally disturbed by typhoons. From September to October 1997, SST levelled off around 29°C. Cooling began in November 1997 and SST dropped from 29°C to 25°C in the following 2 months, reaching the lowest point at the end of 1997. Subsequent warming was almost linear from January to April 1998, completing an annual cycle. Moving into the second annual cycle from April 1998 to April 1999, the similar annual cycle was disturbed by fewer typhoons until October 1998. With fewer typhoons in 1998, the August SST was about 2°C higher than in 1997. The minimum SST occurred in February 1999, 1 month later than in the preceding year. Subsequent warming was faster than in the preceding year to complete the annual cycle. The last segment of time series at SCS1, from August 1999 to May 2000, did not cover a whole year and lacked SST. Looking at T25 as an SST replacement, it showed a similar annual cycle as in previous years but internal motions began to emerge at this depth. Further, following T25 throughout the 3-year period, it began to show pronounced intraseasonal variations from the very beginning.

[15] At SCS2, the SST time series followed a similar annual cycle except with smaller amplitude. Also relative to its counterpart at SCS1, the SST at SCS2 was higher during the cooling phase of a year (from September to March). Apparently, the NE monsoon preferentially evaporated and cooled northern SST. The interannual variation was similar to that at SCS1; SST for 1999–2000 was lower relative to 1998–1999.

[16] At SCS3, time series of SST followed similar trends observed at SCS2 and SCS1. Winter cooling was even milder as the SST was the highest among three stations from January to March. In August 1999 (Figure 4c), the unusually low temperature could be induced by intraseasonal motions.

[17] Summarizing, the sea surface of SCS appeared to be mostly isothermal in summer, but preferentially cooled in the north by the NE monsoon in winter. Superimposed on the annual SST cycle were mostly inter- and intra-annual variations, and typhoon-induced disturbances. However, intra-annual variations were not particularly pronounced at the sea surface and, as forthcoming analyses consistently indicate, stood out better at subsurface depths.

3.2.2. Thermocline

[18] At SCS1, temperature at 75 m (T75) was rich in high-frequency and intraseasonal fluctuations (pink lines in Figure 4a). The high-frequency fluctuations were mostly daily while intraseasonal fluctuations were from days to weeks. The annual cycle became faint at this depth. From April 1997 to April 1998, T75 peaked out twice, once in June 1997 and in December 1997, fortuitously suggesting a semiannual cycle. Two prominent peaks aside, intraseasonal fluctuations ranging up to 2–4°C lasted from days to weeks and extended from 50 to 300 m. Moving to the second year (from April 1998 to April 1999), the fortuitous semiannual

Figure 4. (a) Time series of temperature at different depths at SCS1. Color distinguishes measurement depths. Passing typhoons and tropical storms (Victor, Zita, Cass, Hank, Nichole, Penny, Babs, York, Dan, and Eve) are marked on top when they are closest to the buoy. (b) Corresponding features with tropical storm Eve at SCS2. (c) Corresponding features typhoons Elvis and Faith at SCS3.
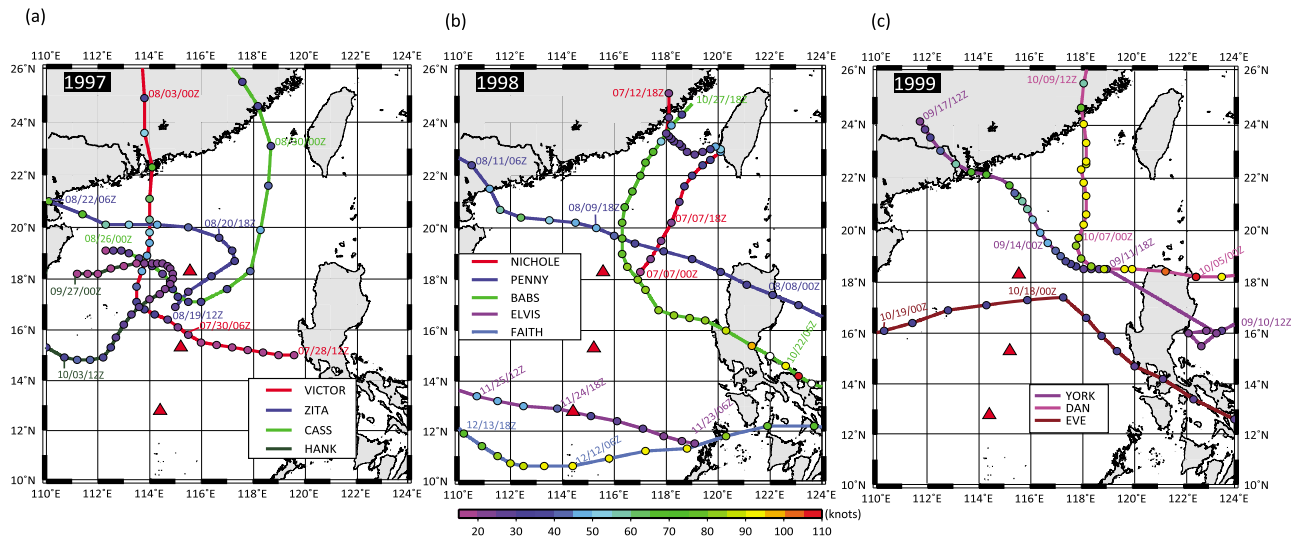
Figure 5. (a) Typhoon and tropical storm tracks dotted 6-hourly in 1997 and buoy locations (red triangles). Dot color indicates maximum wind speed in knots. Victor and Zita are Category 1; Cass and Hank are tropical storms. (b) Corresponding features in 1998: Nichole, Penny, and Elvis, tropical storms; Babs, Category 4; Faith, Category 2. (c) Corresponding features in 1999: York, Category 1; Dan, Category 3; Eve, tropical storm.

cycle in the preceding year disappeared. Instead of two prominent peaks, typhoon Babs induced a month-long 6°C drop at T75, surprisingly larger than the corresponding drop in SST. Thereafter T75 rebounded quickly in the beginning of December. As in the preceding year, T75 reached maximum toward the end of December 1998. Subsequent rapid cooling, 3–4°C less than in the preceding year, was followed by slow warming beginning in February 1999. From August 1999 to May 2000, daily fluctuations at T75 decreased in amplitude. Intraseasonal variations, about 4–6°C in amplitude, were larger than in the previous two years. Interannual dissimilarities aside, one transcending similarity was the somewhat counterintuitive winter warming of T75, which could have been caused by strong NE monsoon induced mixed layer deepening.

[19] At SCS2, the evolution of T75 from 1998 to 1999 generally followed SST (Figure 4b). Time series of T75 at SCS2 and SCS1 were considerably different. The two were almost out of phase from April 1998 to April 1999. The former was generally high while the latter was low from June to October 1998. From April 1998 to April 1999, the mean T75 at SCS2 was 2.5°C higher than at SCS1. The range of variation for T75 exceeded 9°C at SCS2 while it was only 6°C at SCS1 over the yearly period. Intraseasonal and daily fluctuations still dominated at SCS2, ranging up to 4°C and 2–4°C, respectively. From August 1999 to May 2000, the range of variation for T75 at SCS2 (21–27°C) was not as high as in the first segment of measurement, but the temporal variation was alike. The seasonal signal was mostly missing. In contrast to winter warming at SCS1, T75 at SCS2 cooled in both winters.

[20] For the first-year measurement at SCS3, T75 differed somewhat from that at SCS2. For example, from April to June 1998, the former went from cooling to warming while the latter went from warming to cooling. In September and October, T75 at SCS3 dropped sharply twice while it was a

gradual decrease at SCS2. In February 1999, a sudden 7°C warming at SCS3 accounted for the maximum range of variation for the first segment of measurement, while it was cooling at SCS2. Daily fluctuations at SCS3, around 1–3°C, persisted throughout the first segment. For the second segment of measurement (from August 1999 to May 2000), T75 at SCS3 reached a record low in August 1999 among all time series at both SCS2 and SCS3, followed by 9°C warming to reach the maximum. Thereafter, variations became similar to that at SCS2 until February 2000, after which T75 remained low to the end.

[21] Summarizing, winter (November to January) temperature in the thermocline increased at SCS1 but decreased at SCS2 and SCS3. Daily fluctuations showed interannual variations at SCS1, decreasing in the last segment of measurement. At SCS2 and SCS3, daily fluctuations persisted throughout. Energetic intraseasonal variations persisted in the thermocline at all three stations. The annual cycle became faint in the thermocline. Among all three stations, mean T75 was generally the highest at SCS2 and lowest at SCS1.

3.2.3. Below the Thermocline

[22] Temperature variations decayed below the thermocline. Looking at T300 at SCS1, it generally followed the evolution of T75. The mean temperature was about 11°C for all measurements and the daily fluctuation was about 1°C. Judging from vertical temperature gradient, 1°C fluctuation at 300 m equalled about 20 m vertical displacement. There was no clear annual variation. Intraseasonal fluctuations of T300, ranging up to 2°C, could be traced back to the upper ocean. From March to April 2000, a warming spurt of 2°C was the largest variation of T300.

[23] Moving from SCS1 to SCS2, the mean T300 was 0.5°C higher; daily and intraseasonal fluctuations also became smaller. Unlike the thermocline, T300 varied little from 1998 to 1999. Some intraseasonal signals mimicked
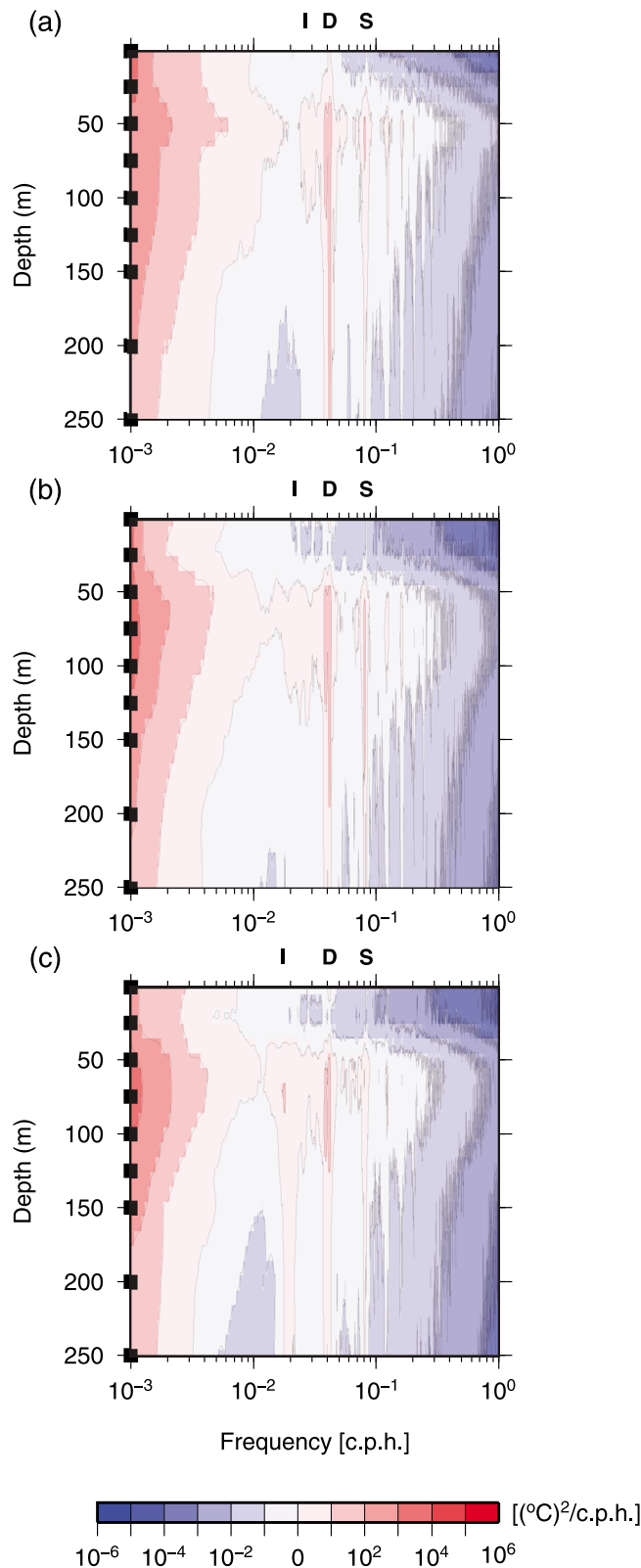
Figure 6. Variance spectrum of temperature in the top 250 m from April 1998 to April 1999 at (a) SCS1, (b) SCS2, and (c) SCS3. Solid squares on left are measurement depths. Marked on top (S, D, and I) are semidiurnal, diurnal, and inertial frequency, respectively. The inertial period is 38.3 h at SCS1, 45.4 h at SCS2, and 54.7 h at SCS3.

that at T75 with smaller amplitude, notably from May to September 1998. Some were unresponsive to corresponding thermocline fluctuations, notably from November 1998 to February 1999 and from March to April 2000.

[24] At SCS3, T300 co-oscillated with that at SCS2. Basin-scale motions might be the cause. Difference was also noticeable. From August to the end of October 1999, for example, T300 at SCS2 was in a warm phase while it reached the lowest value at SCS3. Generally, signals at SCS2 and SCS3 were coherent, and stronger than that at SCS1.

3.2.4. Typhoon-induced Variations

[25] Figure 5 shows the track, timing, and strength of all tropical storms and typhoons during observations. Tropical storms and typhoons induced changes in SST lasting from days to months. The impact from each typhoon was unique. For example, most of tropical storms did not decrease T25 but Eve caused it to drop by 2.5°C at SCS1 in October 1999. The cold anomaly lingered on until the end of November. Victor, a category 1 typhoon, caused strong mixing of upper 50 m in July 1997, cooling SST but warming T50. Zita (category 1), on the other hand, decreased both SST and T50. Weaker upper-ocean stratification during Zita could make the difference. Another category 1 typhoon, York, induced a meager (1°C) drop of T25 at SCS1 in mid-September 1999. The mooring location relative to the typhoon tracks could make the difference, noting that SCS1 was on the right of Victor track but on the left of York track (Figures 5a and 5c). In October 1999, Dan (category 3), though 250 km away from SCS1, caused its T25 to drop by 2.5°C in a burst. Typhoon Babs (category 4), the strongest during measurements, exerted its impact at SCS1 down to 500 m at the end of October 1998. SST and T25 dropped suddenly by 4°C and stayed there for about 2 months. T50 even dropped by more than 7°C briefly. Obviously, the oceanic response varied with typhoon intensity, track, and ocean preconditioning. Two typhoons, Elvis and Faith, followed southern routes but had little impact on SCS3 temperature. The former might be too weak while the latter might be too remote.

4. Analysis

[26] Using raw time series from April 1998 to April 1999, Figure 6 shows the variation of energy spectrum density with depth at all three stations. Diurnal and semidiurnal peaks stand out at all depths and all stations. The former is larger than the latter. Both concentrated in depths from 25 to 200 m and the depth range decreased from SCS1 to SCS3. The spectrum contours confirmed the basinwide internal tidal motions. Internal inertial oscillations, though weaker, also stood out. Unlike internal tide peaks, the near inertial peak was highest at SCS3. Conceivably, typhoons Elvis and Faith (Figure 5) could have caused the southern bias.

[27] The Brunt-Väisälä frequency square (N^2, Figure 7) pretty much defined the thermocline. Following the maximum N^2 at SCS1, the thermocline was shallow and strong in summer but deep and weak in winter. Reduced insolation and strong wind mixing all winter long could conceivably cause the seasonal difference. Among the three winters, N^2 at SCS1 was the strongest and shallowest from 1997 to 1998, apparently due to weak NE monsoon during the El
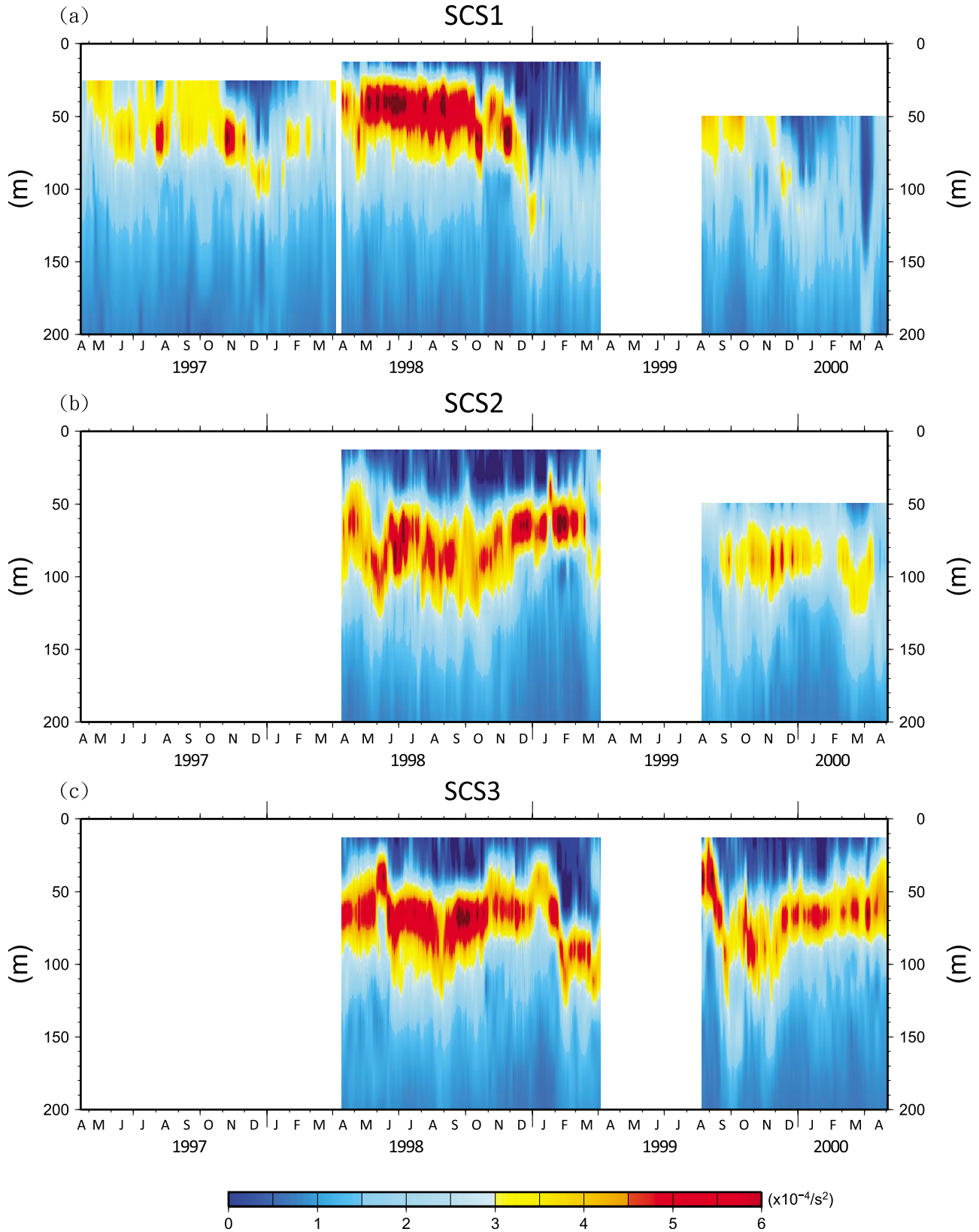
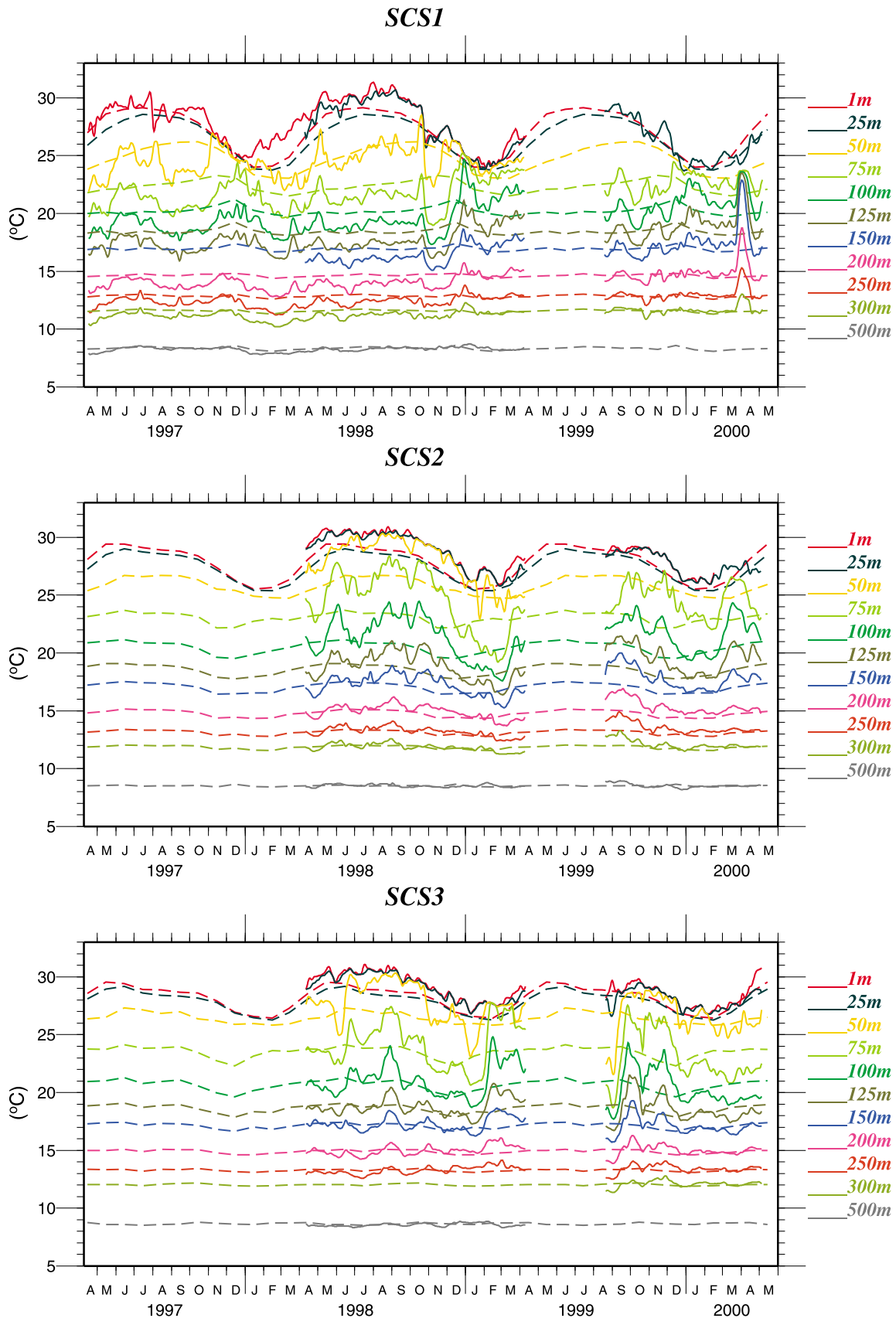**Figure 7.** Brunt-Väisälä frequency square (N^2) in the top 200 m at (a) SCS1, (b) SCS2, and (c) SCS3.

Figure 8. Time series (solid curves) of 96 h low-passed temperature at different depths at (a) SCS1, (b) SCS2, and (c) SCS3. Superimposed are corresponding time series (dashed curves) from World Ocean Atlas 2005 (WOA05).
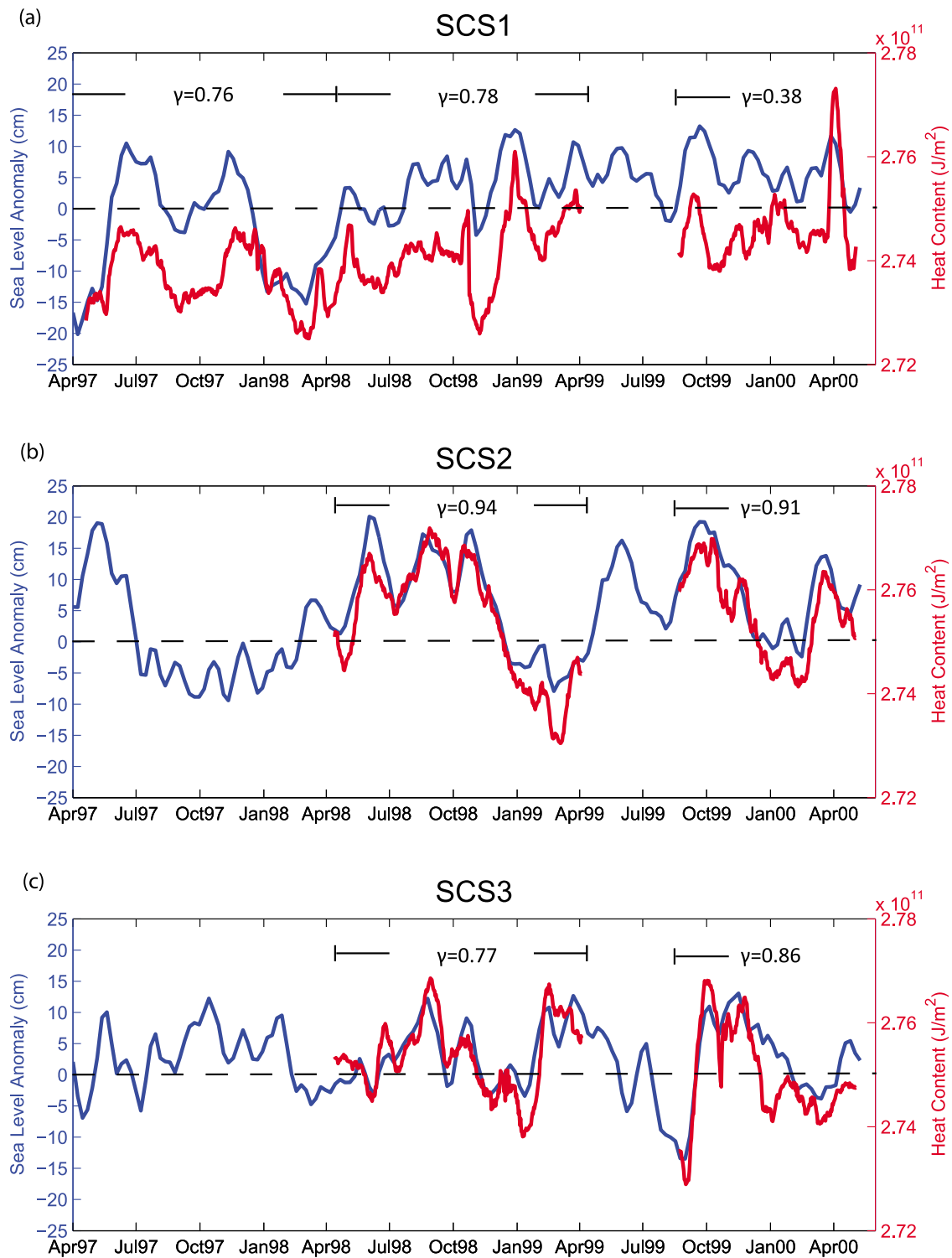
Figure 9. Heat content (red curves) in the top 250 m at (a) SCS1, (b) SCS2, and (c) SCS3, superimposed on sea level anomaly (SLA) time series (blue curves) derived from archiving, validation, and interpretation of satellite oceanographic data (AVISO). Black dash line is a reference for zero SLA. On top is the correlation coefficient (γ) between heat content and SLA in each measurement period.

Niño event (Figure 3). Typhoons acted differently mostly because they were short and strong pulses. They mixed the upper ocean and compressed the thermocline downward, resulting in stronger posttyphoon thermocline instead. Moving from SCS1 to SCS2, one sees a different season-

ality with the maximum N^2 deeper in summer and shallower in winter. At SCS3, seasonality was not well defined. From April 1998 to April 1999, the thermocline was shallower in summer and deeper in winter, similar to that at SCS1. Two shallowest peaks occurred in June and January in this
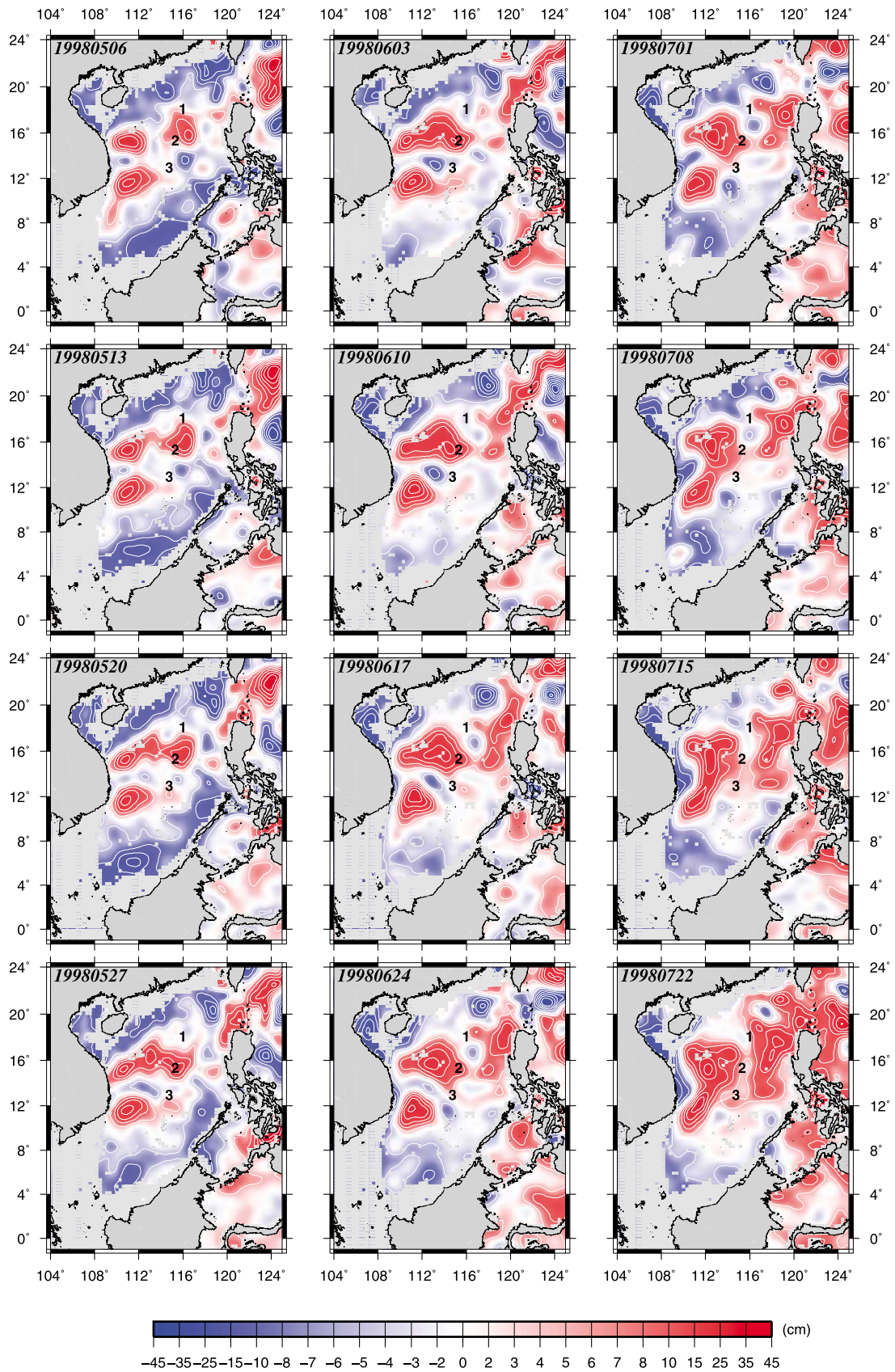
Figure 10. AVISO sea level anomalies (SLA) from 6 May to 22 July 1998 at 7 d intervals. The sequence is from top to bottom and then from left to right. Buoy locations are labeled as 1, 2, and 3. Gray shading indicates areas shallower than 200 m.
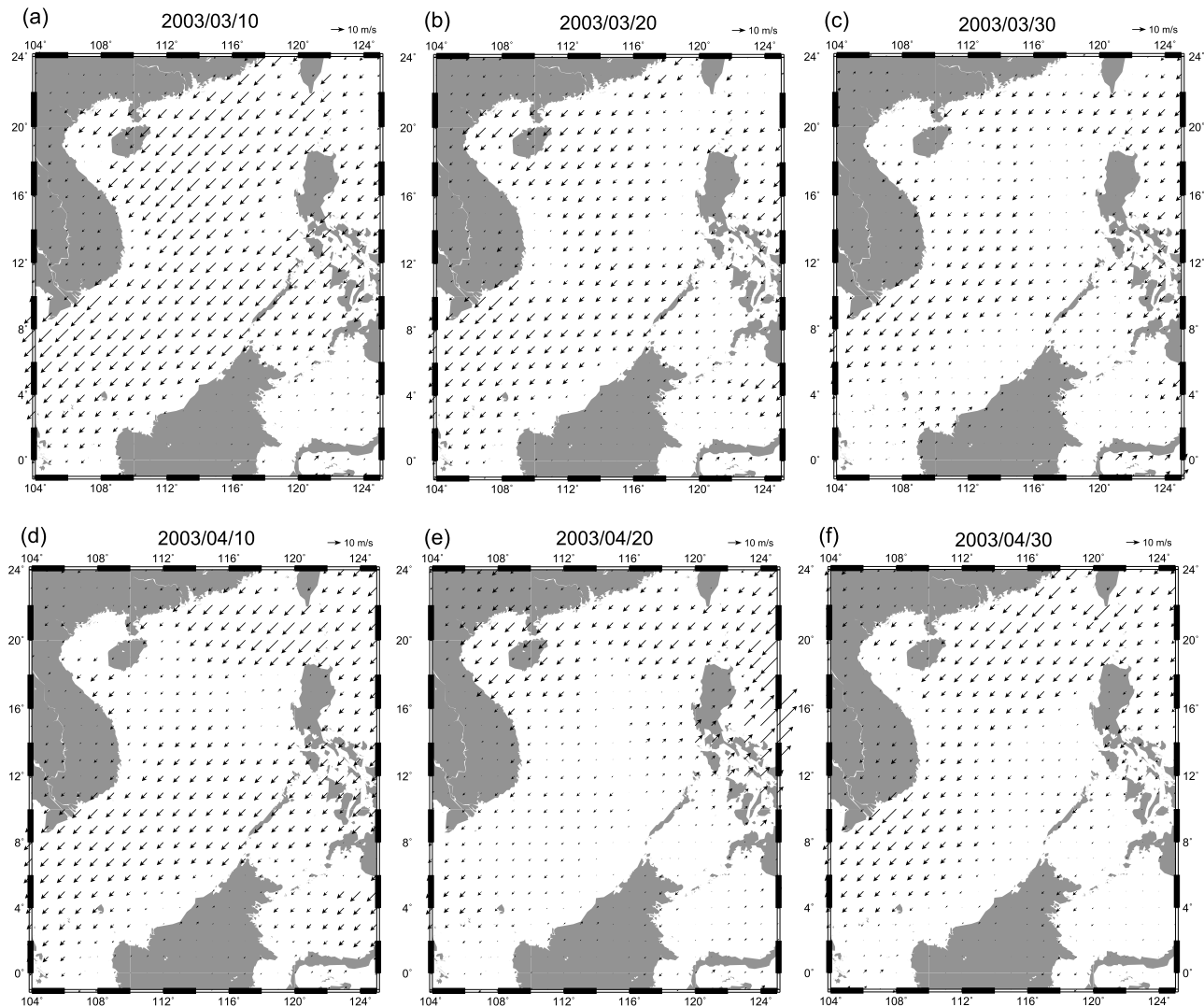
Figure 11. Wind fields from Navy Operational Global Atmospheric Prediction System (NOGAPS) on (a) 10 March, (b) 20 March, (c) 30 March, (d) 10 April, (e) 20 April, and (f) 30 April.

period. From August 1999 to May 2000, however, the winter deepening from October to November gradually rebounded thereafter, sooner than the preceding year. Among three stations, thermocline is the shallowest at SCS1, above 40 m in summer.

[28] To accentuate intraseasonal and interannual variations, we further smoothed the time series by a 96h low-pass filter and compared it with corresponding climatology from WOA05 [World Ocean Atlas 2005, *Locarnini et al.*, 2006]. WOA05 was constructed with historical oceanographic temperature profiles from the National Oceanographic Data Center/ World Data Center (NODC/WDC) archives. Figure 8 shows the result. Climatologic temperature at all stations was high in summer and low in winter. It peaked in July at SCS1 but in early April at SCS2 and SCS3. At SCS3, higher insolation and reduced winter cooling by the NE monsoon raised the climatologic temperature mostly in the upper 100 m. Due mostly to the enhanced winter cooling by NE monsoon in the north, the seasonal variation of climatologic SST decreased southward, from 5°C at SCS1 to 2.5°C at SCS3.

[29] Our time series often deviated from climatology markedly. At SCS1, temperature in the mixed layer (1 and 25 m) agreed with climatology in 1997 but was much higher mostly in 1998. It returned to climatology after typhoon Babs. Thereafter T25 followed climatology in 1999 and 2000. From 50 to 300 m, hereafter referred to as subsurface, variations were similar but attenuated with depth. In 1997, the subsurface temperature deviated from climatology most of the time. Winter warming, lasting longer above 200 m, brought data closer to climatology. However, this warming event did not last long beneath 200 m. In mid-December 1997, Kuroshio intrusion shed an anticyclonic eddy, which became better defined in mid-January 1998 [*Caruso et al.*, 2006]. The eddy then propagated southwestward possibly through SCS1. Their eddy sighting was from sea surface (SST and surface geostrophic velocity). Subsurface warming at SCS1 occurred 1 month earlier, possibly because subsurface signals were much better developed.

[30] From November 1997 to December 1998, T50 at SCS1 agreed better with climatology (Figure 8a). Relative to climatology, temperatures in this period were higher above
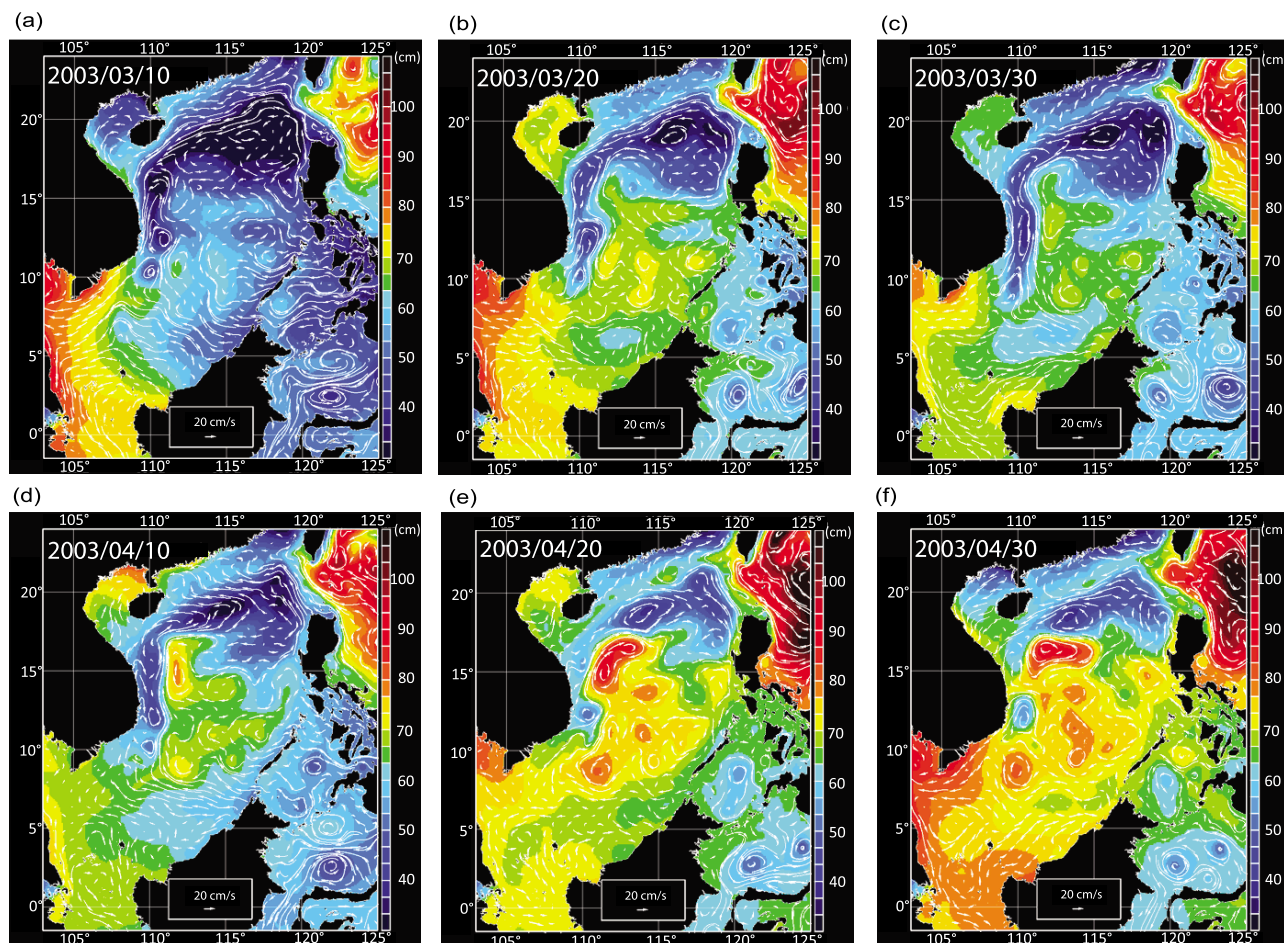
Figure 12. Sea surface height contours and currents (white arrows) from East Asian Sea Ocean Now-cast/Forecast System (EASNFS) on (a) 10 March, (b) 20 March, (c) 30 March, (d) 10 April, (e) 20 April, and (f) 30 April in 2003.

50 m and lower below. Subsurface temperatures were lower than climatology but not as much as in 1997. Typhoon Babs brought a reversal. Thereafter the observed subsurface temperature was higher than climatology. From August 1999 to May 2000, subsurface deviations from climatology were modest except for a warm burst from March to April 2000. Mesoscale phenomena such as a warm eddy passing could have produced it. The 1997–1998 El Niño also played a role, raising SST much above climatology in 1998. However, subsurface warming above climatology was not as clear from 50 m down.

[31] Moving from SCS1 to SCS2, our time series departed from climatology farther (Figure 8b). The seasonal variation of climatology in upper 200 m was far too gentle. Looking at the maximum deviation from climatology, T75 was up to 5°C higher in summer 1998 and lower by as much as 3.5°C in winter. From the sea surface down, the climatologic isothermal layer thickness in winter was usually 25 m but occasionally up to 50 m. Corresponding thickness was often 50 m from our observations. The subsurface winter cooling was missing from climatology at SCS2, most likely due to data paucity. From August 1999 to May 2000, our observed subsurface temperature at SCS2 peaked in September and March; subsurface winter cooling in between was still in place. However, warming started in mid-February 2000,

about half a month earlier than the preceding year. It subsequently raised the subsurface temperature by as much as 2.5°C in 1.5 months.

[32] At SCS3, the surface isothermal layer thickness was often 50 m but reached 75 m in 1998–1999 winter (Figure 8c). SST still retained seasonal cycle. Down below, subsurface signals became highly aperiodic throughout. Several in-traseasonal fluctuations stood out from April 1998 to April 1999; each lasted for about 1 month and induced 3–4°C variation at subsurface depths. Also from our observations, intra-seasonal fluctuations largely subsided after 1999–2000 winter. The climatology failed to represent SCS3, especially before 1999–2000 winter, mostly because of its inability to capture energetic intraseasonal fluctuations.

[33] The predominance of intraseasonal variations in and above thermocline indicates possible links to mesoscale eddies as documented in *Chu et al.* [1998], *Hwang and Chen* [2000], and *Wang et al.* [2003]. To verify, we depth-integrated upper ocean heat content (HC) over the top 250 m and compared it with sea level anomaly (SLA) derived from archiving, validation, and interpretation of satellite oceanographic data (AVISO). The correlation coefficient (γ) was predictably high except for the last segment of measurement (from August 1999 to May 2000) at SCS1 (Figure 9). At the highest, γ was over 0.9 at SCS2.
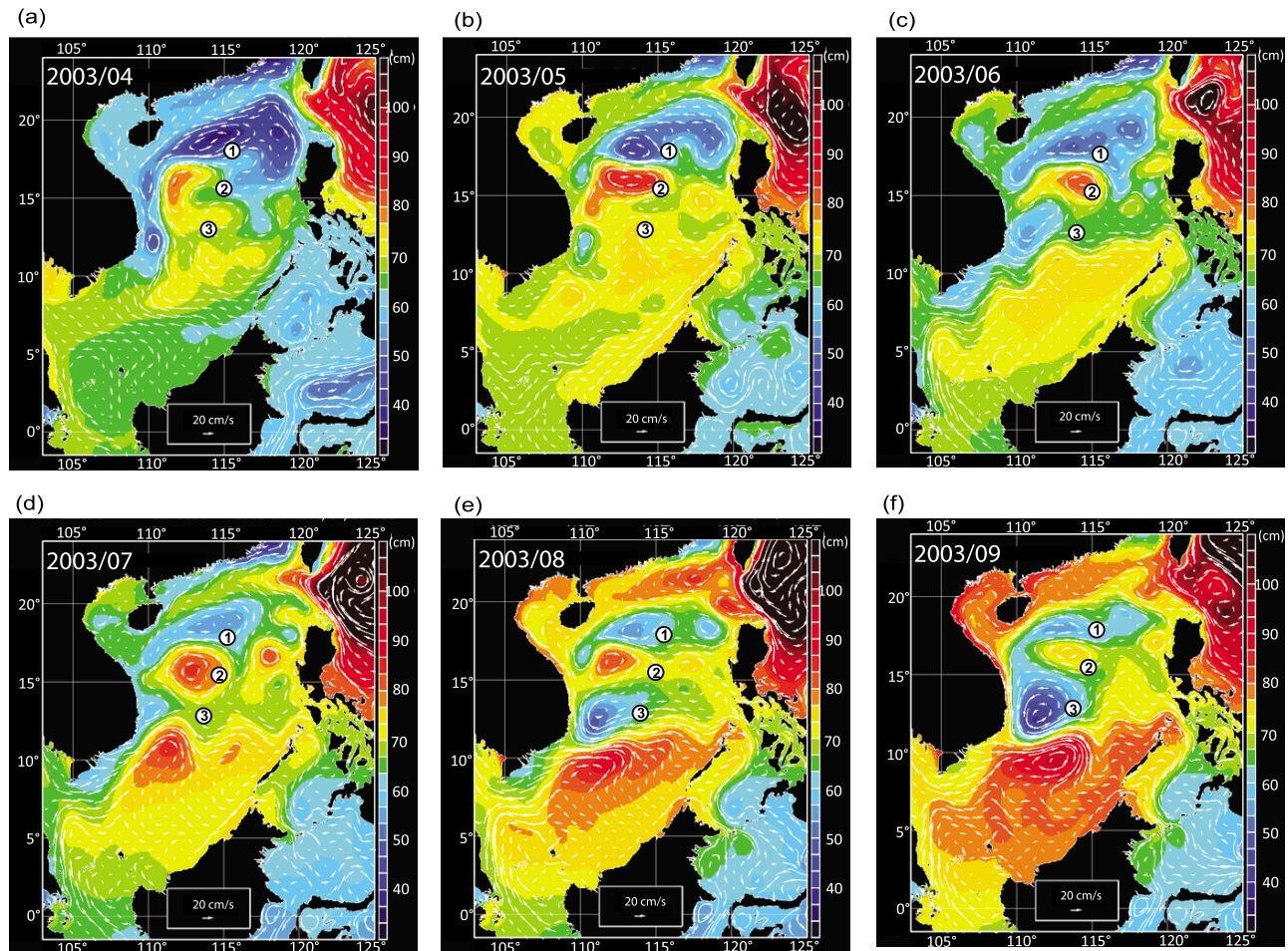
Figure 13. Same as Figure 12 except for monthly averages in (a) April, (b) May, (c) June, (d) July, (e) August, and (f) September of 2003. Buoy locations are labeled as 1, 2, and 3.

On average, γ was the lowest at SCS1, indicating increased contributions from ageostrophic and noneddy processes in the vicinity.

[34] Temporally, HC and SLA at SCS1 showed a relative low before April 1998. Thereafter typhoon Babs in late October 1998 induced a sizable (over 2×10^9 J/m^2) loss in HC and a 10 cm SLA drop. More than a year later, HC peaked prominently (by over 3×10^9 J/m^2) in March–April 2000 along with a modest SLA rise. Corresponding AVISO map (not shown) indicated warm eddy passing.

[35] At SCS2, HC and SLA were generally high. There were 3 HC peaks along with corresponding SLA peaks in the summer of 1998. To put these warm anomalies in perspective, Figure 10 shows concurrent AVISO maps at 7-day intervals. On 6 May 1998, there were three warm eddies in the SCS, two along the coast of Vietnam and one east of SCS2. In time, the east eddy moved westward at about 7.8 km/d to merge with the northern warm eddy off Vietnam. Further merging with the third eddy was occurring in the last one-third of snapshots of Figure 10. The ever-changing warm anomalies skirted SCS2 all summer long, producing 1998 summer peaks in HC and SLA (Figure 9b). We will further elaborate this point in the next section.

[36] At SCS3, HC and SLA changed profoundly from year to year (Figure 9c), indicating domination of in-traseasonal variations over the annual cycle. Commonalities did exist. For example, peaks during the monsoon transition period (September–October) and winter low from December to January occurred in both years.

5. Discussion

[37] Eddies, especially warm ones, are ubiquitous features vividly seen from altimeter data over the SCS [*Morimoto et al.*, 2000; *Wang et al.*, 2003]. They often occur during or shortly after cessation of the winter NE monsoon [*Wang et al.*, 2003]. The persistence of a warm eddy off central Vietnam (Figure 10) is a notable example, leading to multiple warm events at SCS2 (Figure 9b). According to an earlier numerical model driven by monthly climatology winds [*Chu et al.*, 1998], the cessation of winter (summer) monsoon could lead to a warm (cold) eddy in the central basin. Farther east, a reduced-gravity model [*Wang et al.*, 2008] suggested that winter gap winds between islands could populate eddies near the Luzon Strait. The last mechanism is, however, too far east of our region of interest.

[38] Previous literature and the foregoing analysis suggest the warm eddy in the central-western SCS as a persistent and recurrent feature in each spring–summer period. This inspires us to examine the generation mechanism using
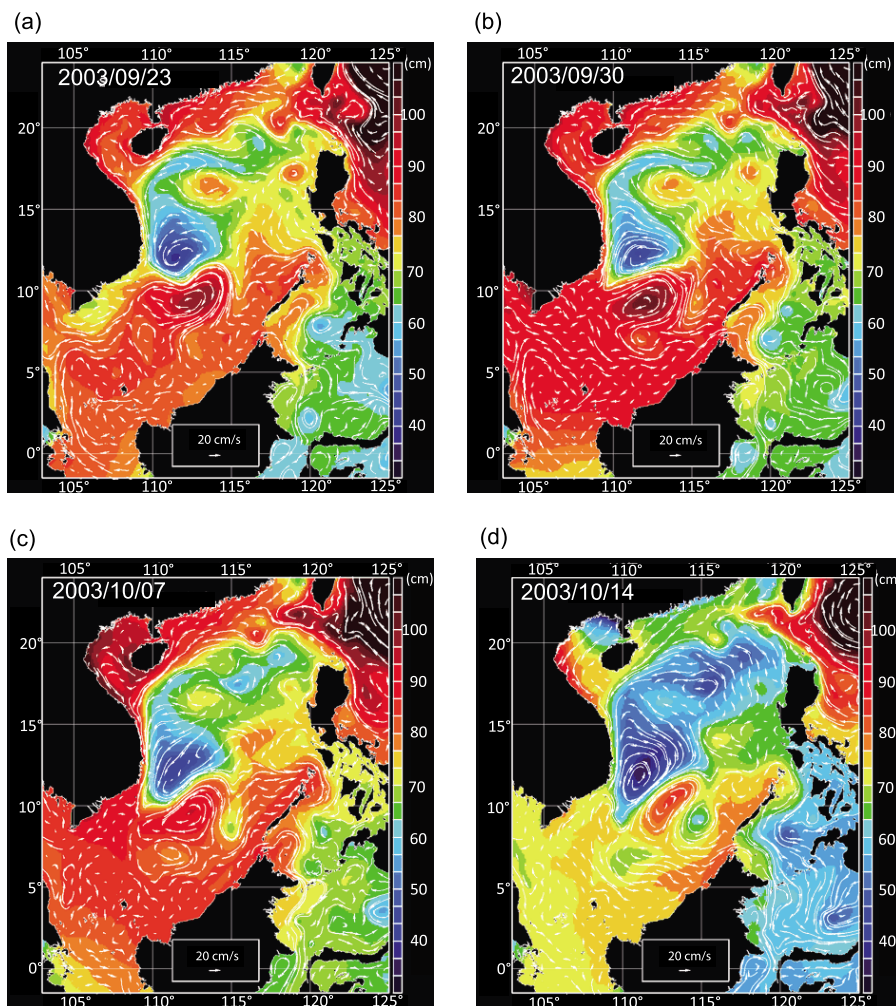
Figure 14. Same as Figure 12 except for (a) 23 September, (b) 30 September, (c) 7 October, and (d) 14 October in 2003.

qualified modeling results from later years, whenever available. Realistic, eddy-resolving simulations of SCS with satellite and hydrographic data assimilations began in 2003 [*Ko et al.*, 2009]. We use archives from 2003 to 2009 to launch discussions below.

[39] The East Asian Seas Nowcast/Forecast System (EASNFS) developed at the U.S. Naval Research Laboratory (NRL) covers the western Pacific and all Asian marginal seas from 17.3°S to 52.2°N and from 99.2°E to 158.2°E with 1/16° resolution. Vertically, there are 11 σ layers in the top 147 m and 29 z layers below. The system is an integration of a data-assimilating dynamic ocean model, a statistical data-analysis model, and various data streams for ocean bathymetry, climatological data, surface forcing, open boundary forcing, and observations for data assimilation [*Ko et al.*, 2008]. The NRL Modular Ocean Data Assimilation System [MODAS; *Carnes et al.*, 1996; *Fox et al.*, 2002] is used within EASNFS as the data analysis model. MODAS uses satellite data, in situ observations and historical statistics to generate three-dimensional ocean temperature and salinity analyses. The analyses are then assimilated into the dynamic model to produce an ocean nowcast. Aiming mostly at open-ocean applications, the system does not

simulate tides. The system derives its ocean bottom topography from the Digital Bathymetry Data Base with 2 min resolution (DBDB2), its open ocean boundary conditions from NRL global Navy Coastal Ocean Model (NCOM) [*Rhodes et al.*, 2002], and its atmospheric forcing from a global weather forecast model (Navy Operational Global Atmospheric Prediction System or NOGAPS) [*Ko et al.*, 2008].

[40] Going over daily archives from 2003 to 2009, we identified monsoon transition periods (March–April and September–October) as the most favorable for warm eddy genesis in the SCS. On average, the spring-generated warm eddy was much longer-lasting than its fall counterpart. Therefore, it is not surprising to see diminishment of warm events after October at SCS2 and SCS3 (Figure 9). To illustrate, we use 2003 archives as a paradigm.

[41] Figure 11 shows snapshots of NOGAPS winds from March to April 2003, essentially at 10-day intervals. This was the cessation period for the winter NE monsoon. The cessation was often interrupted by renewed outbursts. By the end of April, remnants of NE monsoon still existed but faded away intermittently.
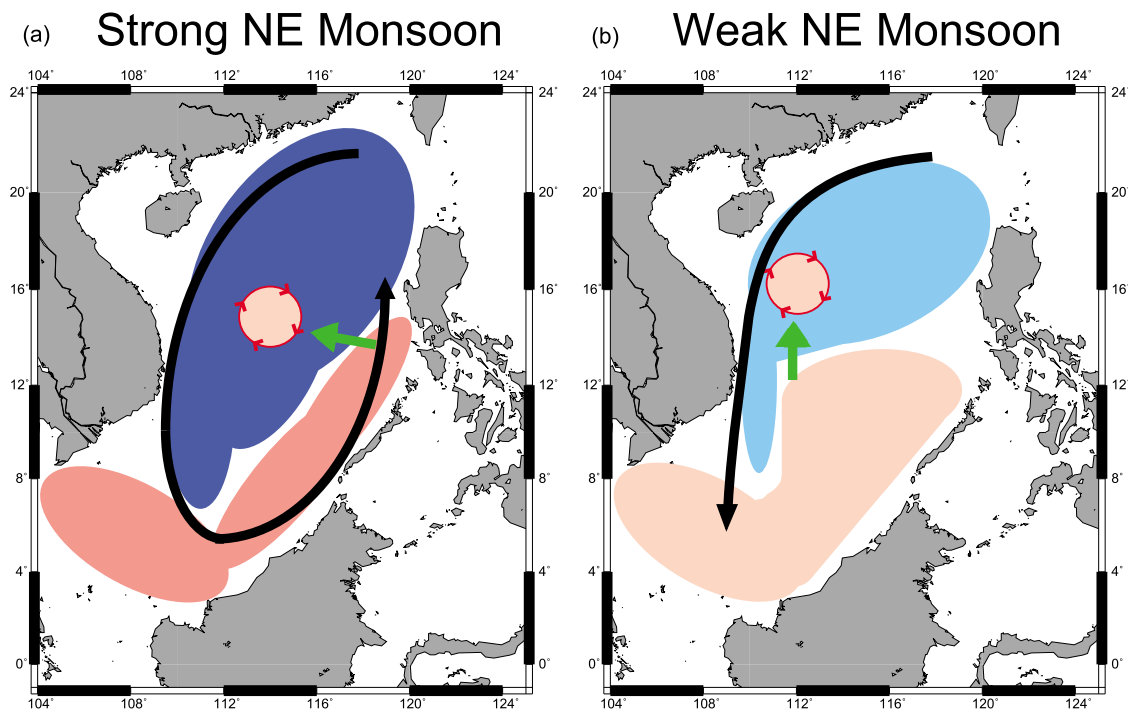
Figure 15. Schematics showing genesis of the spring-summer warm (anticyclonic) eddy in the central South China Sea after (a) a strong NE winter monsoon and (b) a weak NE winter monsoon. Black arrows illustrate basin-scale cyclonic gyres in winter. Darker blue indicates greater sea level depression induced by the winter NE monsoon, whereas darker pink illustrates higher sea level elevation above the mean. Green arrows illustrate warm eddy genesis and subsequent movement.

[42] Figure 12 shows concurrent sea surface heights and currents derived from EASNFS. On 10 March 2003, the sea surface depression in the northern SCS was still expansive. A downwind (southward) coastal jet follows the western boundary of the sea throughout. This was the prevailing winter condition in which the NE monsoon moved and piled up waters to the south. Thereafter the excess water in the south returned as the NE monsoon weakened. Conceivably, the return flow was initially barotropic but quickly becomes surface-trapped because waters from the south were warmer and therefore more buoyant. The initial northward intrusion was away from the western boundary, where remnants of the southward coastal jet prevented its northward migration. This situation also favored warm eddy genesis. On 20 March (Figure 12b), for example, the warm intrusion produced a series of weak anticyclonic (warm) eddies centered along 11°N. The western few soon coalesced and became a dominant warm eddy. By 20 April (Figure 12e), the warm eddy, centered around 112°E and 16°N, was well formed and persisted thereafter. The radius of the warm eddy, about 50 km or so, was comparable to the Rossby radius of the first baroclinic mode, a scale of choice for a warm intrusion event [*Cushman-Roison*, 1994].

[43] To illustrate longevity of the predominant warm eddy, Figure 13 shows monthly averaged sea surface heights and currents from April to September, along with the three ATLAS mooring locations as a reference. The warm eddy moved around the latitude of SCS2, but mostly skirted its western side. It eventually weakened in September, after which the winter NE monsoon began.

[44] Figure 14 shows another anticyclone generation when the monsoon changed from southwest to northeast in fall 2003. Unlike the spring-summer anticyclone, the fall one was shorter in life and bounded in lower latitudes. On September 23 (Figure 14a), the circulation was still summerlike. The summer wind stress curl, positive in the northern basin and negative in the southern basin, produces a double gyre circulation that intensifies along the western boundary [*Chao et al.*, 1996]. In the southern basin, a northward western boundary current departed from the coast and meandered eastward around 11°N or the latitude of zero wind stress curl. North of it was a cyclonic gyre supported by the summer positive wind stress curl. During the transition from summer to winter circulation, the meandering eastward jet around 11°N broke up to form an anticyclonic eddy (Figure 14b). The warm eddy subsequently moved eastward while weakening (Figure 14d), and diminished in December (not shown).

[45] The foregoing (2003) paradigm is subject to interannual variations. Summarizing EASNFS archives from 2003 to 2009, Figure 15 conceptualizes the interannual variations for the genesis of spring–summer warm eddy in the central-western basin. In normal years with a strong winter NE monsoon (Figure 15a), the winter cyclonic gyre is able to go around the southern basin. The warm eddy soon to appear can be generated in the eastern-central basin and subsequently moves westward while intensifying. This occurred in 2006, 2007, 2008, and 2009 (results not shown). A weakened NE monsoon, often caused by El Niño, reduces the counterclockwise expansion of the winter cyclonic gyre (Figure 15b). Subsequent warm eddy generation favors a

southern origin, such as in the case of 2003. There are year-to-year variations between these apparent extremes.

6. Summary

[46] Long-term temperature measurements shed light on the geographical and temporal variability of thermal structures in the SCS. The observations spanned years containing strong El Niño/La Niña events. The basinwide, year-round internal motions stood out as the most remarkable feature in the raw data. From spectral analysis, we further identified active internal tides in a depth range from 25 to 300 m. Typhoons induced temperature drops of varying degrees, depending on their strength, translation speed and proximity, and background oceanic stratification. The temperature drop was often pronounced in SST. Corresponding subsurface temperature might increase or decrease, depending on the mixing depth under each typhoon. Despite strong monsoons, seasonal variation dominated only in the SST and decreased with decreasing latitude. Intraseasonal signals often masked the seasonal cycle at subsurface depths, especially in the southern SCS. As high correlations between upper ocean heat content and sea level anomaly bore out, mesoscale eddies, especially warm ones, were chiefly responsible for the ubiquity of intraseasonal signals. A nowcast/forecast system from Naval Research Laboratory shed light on warm eddy generation mechanisms. Monsoon transition periods favored warm eddy formation. In normal years after a strong NE winter monsoon, a warm eddy formed in the eastern-central basin and subsequently moved westward while intensifying, persisting all summer long. After a weak NE monsoon during El Niño events, piled-up warm waters in the southern basin returned northward, becoming the source of warm eddy motion when the monsoon relaxed. The transition from SW to NE monsoon could also produce warm eddies. The eastward summer jet departing from central Vietnam often broke up during the transition, producing a warm eddy in southern latitudes.

References

Bayler, E. J., and Z. Liu (2008), Basin-scale wind-forced dynamics of the seasonal southern South China Sea gyre, *J. Geophys. Res.*, *113*, C07014, doi:10.1029/2007JC004519.

Beardsley, R. C., T. F. Duda, J. F. Lynch, J. D. Irish, S. R. Ramp, C.-S. Chiu, T.-Y. Tang, Y.-J. Yang, and G. Fang (2004), Barotropic tide in the Northeast South China Sea, *IEEE J. Oceanic Eng.*, *29*(4), pp. 1075–1086.

Caruso, M. J., G. G. Gawarkiewicz, and R. C. Beardsley (2006), Interannual variability of the Kuroshio intrusion in the South China Sea, *J. Oceanogr.*, *62*, 559–575.

Carnes, M. R., D. N. Fox, R. C. Rhodes, and O. M. Smedstad (1996), Data assimilation in a North Pacific Ocean monitoring and pre diction system, *Elsevier Oceanography Series*, *61*, 319–345

Chang, C.-W. J., H.-H. Hsu, C.-R. Wu, and W.-J. Sheu (2008), Interannual mode of sea level in the South China Sea and the roles of El Niño and El Niño Modoki, *Geophys. Res. Lett.*, *35*, L03601, doi:10.1029/2007GL032562.

Chang, M.-H., R.-C. Lien, T. Y. Tang, E. A. D'Asaro, and Y. J. Yang (2006), Energy flux of nonlinear internal waves in northern South China Sea, *Geophys. Res. Lett.*, *33*, L03607, doi:10.1029/2005GL025196.

Chao, S.-Y., P.-T. Shaw, and S. Y. Wu (1996), El Niño Modulation of the South China Sea Circulation, *Prog. Oceanogr.*, *38*, 51–93.

Chu, P. C., H.-C. Tseng, C. P. Chang, and J. M. Chen (1997), South China Sea warm pool detected in spring from the Navy's master oceanographic observational data set (MOODS), *J. Geophys. Res.*, *102*(C7), 15761–15771.

Chu, P. C., Y. Chen, and S. Lu (1998), Wind-driven South China Sea deep basin warm-core/cool-core eddies, *J. Oceanogr.*, *54*, 347–360.

Chu, P. C., J. M. Veneziano, C. Fan, M. J. Carron, and W. T. Liu (2000), Response of the South China Sea to Tropical Cyclone Ernie 1996, *J. Geophys. Res.*, *105*(C6), 13991–14009.

Cushman-Roison, B. (1994), Fronts, jets and vortices, in *Introduction to Geophysical Fluid Dynamics*, pp. 240–263, Prentice Hall, Englewood Cliffs, New Jersey.

Duda, T. F., J. F. Lynch, J. D. Irish, R. C. Beardsley, S. R. Ramp, C.-S. Chiu, T. Y. Tang, and Y.-J. Yang (2004), Internal tide and nonlinear internal wave behavior at the continental slope in the northern South China Sea, *IEEE J. Oceanic Eng.*, *29*(4), 1105–1130.

Fang, G. H., Y. K. Kwok, K. J. Yu, and Y. H. Zhu (1999), Numerical simulation of principal tidal constituents in the South China Sea, Gulf of Tonkin and Gulf of Thailand, *Cont. Shelf Res.*, *19*, 845–869.

Fox, D. N., W. J. Teague, C. N. Barron, and M. R. Carnes (2002), The Modular Ocean Data Assimilation System (MODAS), *J. Atmos. Oceanic Technol.*, *19*, 240–252.

Hwang, C., and S.-A. Chen (2000), Circulations and eddies over the South China Sea derived from TOPEX/Poseidon altimetry, *J. Geophys. Res.*, *105*(C10), 23943–23965.

Jan, S., C.-S. Chern, J. Wang, and S.-Y. Chao (2007), Generation of diurnal K1 internal tide in the Luzon Strait and its influence on surface tide in the South China Sea, *J. Geophys. Res.*, *112*, C06019, doi:10.1029/2006JC004003.

Ko, D. S., P. J. Martin, C. D. Rowley, and R. H. Preller (2008), A real-time coastal ocean prediction experiment for MREA04, *J. Mar. Syst.*, *69*, 17–28.

Ko, D. S., S.-Y. Chao, P. Huang, and S. F. Lin (2009), Anomalous upwelling in Nan Wan: July 2008, *Terr. Atmos. Ocean. Sci.*, *20*(6), 839–852.

Lin, I.-I., W. T. Liu, C.-C. Wu, J. C. H. Chiang, and C.-H. Sui (2003), Satellite observations of modulation of surface winds by typhoon-induced upper ocean cooling, *Geophys. Res. Lett.*, *30*(3), 1131, doi:10.1029/2002GL015674.

Locarnini, R. A., A. V. Mishonov, J. I. Antonov, T. P. Boyer, and H. E. Garcia (2006), *World Ocean Atlas 2005, Volume 1: Temperature*, edited by S. Levitus, NOAA Atlas NESDIS 61, U.S. Government Printing Office, Washington, D. C., 182 pp.

Lynch, L. F., S. R. Ramp, C.-S. Chiu, T. Y. Tang, Y.-J. Yang, and J. A. Simmen (2004), Research highlights from the Asian Seas International Acoustics Experiment in the South China Sea, *IEEE J. Oceanic Eng.*, *29*(4), 1067–1074.

Mazzega, P., and M. Bergé (1994), Ocean tides in the Asian semienclosed seas from TOPEX/POSEIDON, *J. Geophys. Res.*, *99*(C12), 24867–24881.

McPhaden, M. J., A. J. Busalacchi, R. Cheney, J. R. Donguy, K. S. Gage, D. Halpern, M. Ji, P. Julian, G. Meyers, G. T. Mitchum, P. P. Niiler, J. Picaut, R. W. Reynolds, N. Smith, and K. Takeuchi (1998), The Tropical Ocean-Global Atmosphere (TOGA) observing system: A decade of progress, *J. Geophys. Res.*, *103*, 14169–14240.

Milburn, H. B., and P. D. McLain (1986), ATLAS: A low cost satellite data telemetry mooring developed for NOAA's Climate Research Mission, in *Proceedings, MDS '86, Marine Data Systems International Symposium*, 30 April—2 May, New Orleans, LA, pp. 393–396.

Morimoto, A., K. Yoshimoto, and T. Yanagi (2000), Characteristics of sea surface circulation and eddy field in the South China Sea revealed by satellite altimetric data, *J. Oceanogr.*, *56*(3), 331–344.

Niwa, Y., and T. Hibiya (2004), Three-dimensional numerical simulation of M2 internal tides in the East China Sea, *J. Geophys. Res.*, *109*, C04027, doi:10.1029/2003JC001923.

Price, J. F. (1981), Upper ocean response to a hurricane, *J. Phys. Oceanogr.*, *11*(2), 153–175.

Price, J. F., T. B. Sanford, and G. Z. Forristall (1994), Forced stage response to a moving hurricane, *J. Phys. Oceanogr.*, *24*(2), 233–260.

Qu, T. (2000), Upper-layer circulation in the South China Sea, *J. Phys. Oceanogr.*, *30*, 1450–1460.

Ramp, S. R., T. Y. Tang, T. F. Duda, J. F. Lynch, A. K. Liu, C.-S. Chiu, F. L. Bahr, H.-R. Kim, and Y.-J. Yang (2004), Internal solitons in the northeastern South China Sea: Part I. Sources and deep water propagation, *IEEE J. Oceanic Eng.*, *29*(4), 1157–1181.

Rhodes, R. C., H. E. Hurlburt, A. J. Wallcraft, C. N. Barron, P. J. Mar tin, O. M. Smedstad, S. Cross, E. J. Metzger, J. Shriver, A. Kara, and D. S. Ko (2002), Navy real-time global modeling system, *Oceanography*, *15*, 29–43.

Shaw, P. T., and S. Y. Chao (1994), Surface circulation in the South China Sea, *Deep-Sea Res. I*, *40*(11/12), 1663–1683.

Shaw, P.-T., S.-Y. Chao, K.-K. Liu, S.-C. Pai, and C.-T. Liu (1996), Winter upwelling off Luzon in the northeastern South China Sea, *J. Geophys. Res.*, *101*(C7), 16435–16448.

Tseng, Y. H., S. Jan, D. E. Dietrich, I. I. Lin, Y.-T. Chang, and T. Y. Tang (2010), Modeled oceanic response and sea surface cooling to typhoon Kai-Tak, *Terr. Atmos. Ocean. Sci.*, *21*, 85–98, doi:10.3319/TAO.2009.06.08.02(IWNOP).

Uppala, S. M., et al. (2005), The ERA-40 re-analysis. *Quart. J. R. Meteorol. Soc.*, *131*, 2961–3012. doi:10.1256/qj.04.176.

Wang, G., J. Su, and P. C. Chu (2003), Mesoscale eddies in the South China Sea observed with altimeter data, *Geophys. Res. Lett.*, *30*(21), 2121, doi:10.1029/2003GL018532.

Wang, G., D. Chen, and J. Su (2008), Winter eddy genesis in the eastern South China Sea due to orographic wind jets, *J. Phys. Oceanogr.*, *38*, 726–732.

Wang, L., C. J. Koblinsky, and S. Howden (2000), Mesoscale variability in the South China Sea from the TOPEX/Poseidon altimetry data, *Deep-Sea Res. I*, *47*, 681–708.

Wu, C.-R., and C.-W. J. Chang (2005), Interannual variability of the South China Sea in a data assimilation model, *Geophys. Res. Lett.*, *32*, L17611, doi:10.1029/2005GL023798.

Wu, C.-R., and T.-L. Chiang (2007), Mesoscale eddies in the northern South China Sea, *Deep Sea Research II*, *54*, 1575–1588.

Wu, C.-R., T. Y. Tang, and S. F. Lin (2005), Intra-seasonal variation in the velocity field of the northern South China Sea, *Cont. Shelf Res.*, *25*, 2075–2083.

Wyrtki, K. (1961), Physical oceanography of the Southeast Asian water. In *NAGA Report Vol. 2, Scientific Result of Marine Investigation of the South China Sea and Gulf of Thailand 1959–1961*, 195 pp., Scripps Institution of Oceanography, La Jolla, California.

Xie, S.-P., Q. Xie, D. Wang, and W. T. Liu (2003), Summer upwelling in the South China Sea and its role in regional climate variations, *J. Geophys. Res.*, *108*(C8), 3261, doi:10.1029/2003JC001867.

Yanagi, T., T. Takao, and A. Morimoto (1997), Co-tidal and co-range charts in the South China Sea derived from satellite altimetry data, *La mer*, *35*, 85–94.

M.-H. Chang, Department of Marine Environmental Informatics, National Taiwan Ocean University, 2 Pei-Ning Road, Keelung, Taiwan 20224.

Y.-T. Chang and T. Yung Tang, Institute of Oceanography, National Taiwan University, Roosevelt Road, Taipei 106, Taiwan.

S.-Y. Chao, Horn Point Laboratory, University of Maryland Centers for Environmental Science, 2020 Horns Point Road, Cambridge, MD 21613, USA.

Y. Jang Yang and W.-D. Liang, Department of Marine Science, Naval Academy, Kaohsiung City 813, Taiwan.

D. S. Ko, Naval Research Laboratory, Oceanography Division, Ocean Dynamics and Prediction Branch, Stennis Space Center, MS 39529, USA.

M. J. McPhaden, Pacific Marine Environmental Laboratory, National Ocean and Atmosphere Administration, 7600 Sand Point Way NE, Seattle, WA 98115, USA.